Strategic alloy design and processing for improved mechanical response in the Mo-Si-Ti system

R.J. Vikram [a,b], Daniel Schliephake [a,*], Manoja Namadi [b], Abhik Choudhury [b], Alexander Kauffmann [a], Satyam Suwas [b], Martin Heilmaier [a]

[a] Institute for Applied Materials (IAM-WK), Karlsruhe Institute of Technology (KIT), Engelbert-Arnold-Str. 4, 76131 Karlsruhe, Germany
[b] Department of Materials Engineering, Indian Institute of Science, Bangalore 560012, India

ARTICLE INFO

ABSTRACT

This study focuses on the impact of off-eutectic microstructures on mechanical properties in ternary Mo-Si-Ti alloys, namely Ti-rich Mo-18Si-72Ti and Mo-16.5Si-72Ti, in relation to the well-researched eutectic, two-phase Mo-20Si-52.8Ti alloy. The microstructure of these alloys consists of a Ti-rich body-centered cubic solid solution $(Ti,Mo,Si)_{ss}$ and a hexagonal silicide phase $(Ti,Mo)_5Si_3$. Notably, the off-eutectic alloys exhibit remarkable compression ductility at 800 °C, distinguishing it from Mo-20Si-52.8Ti. The directionally solidified (DS) specimens of the Ti-rich alloys display higher strength compared to the arc-melted specimens. This enhanced strength is attributed to the multiple precipitation strengthening events present, despite the increase in the length scale of individual phases which further enhances the fracture toughness.

There is a continual industrial demand for materials that can endure higher temperatures without sacrifices in strength or ductility [1]. Traditional high-temperature alloys, such as Ni or (more recently explored) Co base superalloys, are used close to their precipitate solvus temperatures and despite technical advances, any additional temperature increase is improbable [2,3]. As a result, the development of new structural materials which is capable of tolerating even higher temperatures and boosting thermal efficiency is in great demand [4–6]. Intermetallic compounds, while promising, usually suffer from intrinsic brittleness and poor fracture toughness [7–9]. To increase their toughness, one technique is to combine them with a ductile phase [10–12].

In general eutectic systems enable in-situ composites that could balance strength and ductility [13–15]. Furthermore, eutectics provide highly adjustable microstructures/properties, which depend on processing conditions (such as solidification rates and compositions). Inspired by this concept, we conducted preliminary research on a Mo-Si-Ti alloy (Mo-20Si-52.8Ti in at.%) consisting of a body-centered cubic solid solution and an intermetallic hexagonal silicide phase [16–20].

The study of the aforesaid system results in a nearly equal volume percentage of the two distinct phases. By altering the volume fraction (V_f) towards the ductile phase, we may increase inherent toughness while maintaining high temperature capability, as previously demonstrated in Mo-Si-B alloys [21,22]. In light of this, as compared to the eutectic Mo-20Si-52.8Ti alloy, the current study introduces two novel off-eutectic alloys by decreasing the Si content in favour of Ti (and Mo) content and thus, increasing V_f of the solid solution phase. Besides Mo-20Si-52.8Ti, we manufactured off-eutectic Mo-18Si-72Ti and Mo-16.5Si-72Ti by arc-melting from pure elements, details on the arc-melting process can be found in Ref. [20]. Since fracture toughness depends on the microstructural length scale [23,24], we deliberately increased microstructural length scale by directional solidification (DS). Further details on DS can be found in Ref. [20].

Note that for a better understanding and distinction in what follows, eutectic alloy will be referred to as Eu, off-eutectic compositions with primary phase as bcc and hexagonal phase as OEu-bcc and OEu-hex respectively, the as cast material as AC, the directionally solidified specimens as DS. The Mo-rich BCC_{ss} phase in Eu is described as $(Mo,Ti,Si)_{ss}$ and Ti-rich BCC_{ss} in OEu as $(Ti,Mo,Si)_{ss}$. The order of elements in parentheses represents the main element in that particular phase. The volume fraction of a particular phase (X) will be indicated as $V_f(X)$.

The microstructure was examined using a scanning electron microscopy (SEM, by Carl Zeiss and FEI) in secondary electron (SEM-SE) and backscatter electron (SEM-BSE) mode operated at 20 and 30 kV, respectively. Energy-dispersive X-ray spectroscopy (SEM-EDX) was performed using a Zeiss EVO 50 SEM at 20 kV acceleration voltage.

---

* Corresponding author.
E-mail address: daniel.schliephake@kit.edu (D. Schliephake).

The mechanical behavior of the alloys was investigated using compression, microhardness, and nanoindentation experiments. Uni-axial compression tests for AC and DS (Note: All DS specimens were loaded along the longitudinal direction which typically results in higher strength and hardness [6,25,26] due to efficient load transfer along grain boundaries, while loading along transverse direction may offer more ductility but at the cost of reduced strength and toughness, where the cracks can easily propagate through the continuous brittle phase, such as $(Ti, Mo)_5Si_3$ in the present study. Understanding these directional properties is crucial, but it also comes with the constraint and limitation in extracting a transverse specimen for compression testing from a directionally solidified specimen (which is typically 3 mm in diameter with a length spanning up to 90 mm), making it only feasible to test specimens along longitudinal directions) were performed at 800 °C with a strain rate of 10^{-3} s^{-1} on samples with a diameter of 3 mm and a height of 4.5 mm. The Vickers micro-hardness testing equipment (Future-Tech, FM-810) was used with a 500 gf load for a dwell time of 20 s to probe the hardness of each phase. For statistical purposes, ten indents were taken in each phase. To further understand the toughness of the BCC_{ss} phase, we used a larger force of 10 kgf to induce crack radially from the indentation corner. This indentation was performed with a Qness Q10 + microhardness tester and the crack length was determined by SEM technique. The elastic modulus and hardness of the various phases were determined with a Berkovich nanoindenter (Hysitron Triboindenter). Displacement and load were measured with a precision of 0.1 nm and 0.1 μN, respectively. A maximum load of approximately 8 mN was used and the dwell time at maximum load were kept constant for 5 s.

Fig. 1 represents the liquidus projection of the Mo-Si-Ti phase diagram indicating the expected phases as body-centred cubic $(Mo,Ti,Si)_{ss}$/$(Ti,Mo,Si)_{ss}$ and hexagonal $(Ti,Mo)_5Si_3$. According to the Pandat
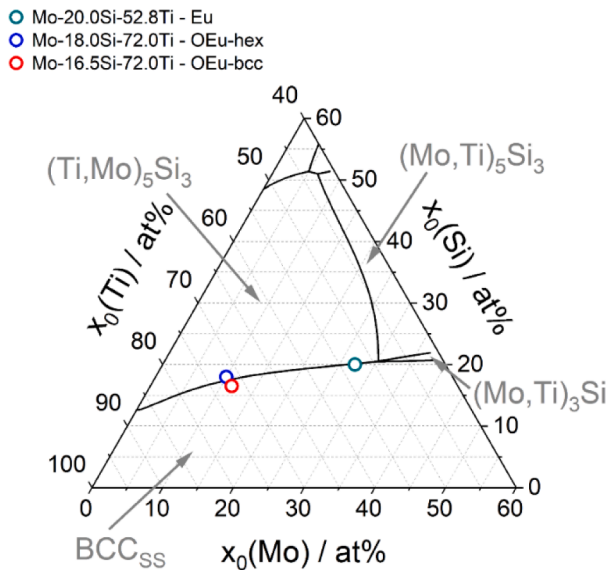

Fig. 1. Liquidus projection of the Mo-Si-Ti phase diagram, calculated using the CALPHAD approach with the PanMo2022 database by Computherm LCC, with three different compositions: eutectic Mo-20Si-52.8Ti as well as off-eutectic Mo-18Si-72Ti and Mo-16.5Si-72Ti. As per the phase diagram, the primary phase that forms is $(Ti,Mo,Si)ss$ in the case of OEu-bcc and $(Ti,Mo)_5Si_3$ phase in the OEu-hex. The Eu has a very high solidus temperature Ts of around 1930 °C and by changing the composition along the eutectic trough Ts decreases to 1750 °C for the OEu. The rationale behind focussing on higher Ti containing alloys stems from the lower solidus temperature of around 1750 °C, and reduced intermetallic phase fraction of $Vf(Ti,Mo)_5Si_3$, while the solidification range (ΔT_L) increases from 205 K to 290 K. Colored symbols representing eutectic (green) and off-eutectic (blue and red) compositions alongside marked their primary phase.

calculations, the $V_f(Ti,Mo)_5Si_3$ decreases to 0.45 and 0.41 for OEu-hex and OEu-bcc, respectively, compared to 0.49 for the Eu alloy. Furthermore, the maximum solubility of Si and Ti in $(Mo,Ti,Si)_{ss}$/$(Ti,Mo,Si)_{ss}$ was calculated for Eu and both OEu alloys. Beside the decreased $V_f(Ti,Mo)_5Si_3$, the solubility limits of Si and Ti in $(Mo,Ti,Si)_{ss}$/$(Ti,Mo,Si)_{ss}$ are changing from 3.9 at.% and 50.2 at.% to 2.5 at.% and 82.3 at.% to 2.5 at.% and 81.1 at.% in Eu and both OEu, respectively. It is important to note, that the solubility of Si decreases with decreasing temperature, while the maximum solubilty of Ti in the OEu alloys is calculated to be at 1300 and 1050 °C for OEu-hex and OEu-bcc, respectively. However, the solubitiy limit of Ti in $(Ti,Mo,Si)_{ss}$ decreases below these temperatures.

The transverse section BSE micrographs of Eu and OEu in AC and DS are displayed in Fig. 2(a–f) which shows the existence of $(Mo,Ti,Si)_{ss}$/$(Ti,Mo,Si)_{ss}$ and silicide $(Ti,Mo)_5Si_3$ exhibiting hexagonal morphology (related to its underlying crystallographic basis) with bright and dark contrast, respectively [27]. The micrographs show eutectic colonies. The relevant microstructural parameters are listed in Table 1. Detailed micrographs of the longitudinal section can be found in the supplementary material. The primary phase is $(Ti,Mo,Si)_{ss}$ and $(Ti,Mo)_5Si_3$ in case of OEu-bcc and OEu-hex, respectively, and is consistent with the assigned primary phase fields in Fig. 1. It is worth noting here, that the microstructure consists of colonies and intercolonies and the primary solidified phase is in the center of each colony [17]. $V_f(Ti,Mo)_5Si_3$ remain similar in all DS conditions compared to AC when considering the experimental errors of 0.02 with respect to its volume fraction and also well reflects the calculated phase fraction by Pandat (see Table 1). $V_f(Ti,Mo)_5Si_3$ decreases from Eu to OEu-hex to OEu-bcc thus increasing the fraction of ductile phase in same order. In addition, the width L of $(Mo,Ti,Si)_{ss}$/$(Ti,Mo,Si)_{ss}$ lamellae and the lamellar spacings λ for $(Mo,Ti,Si)_{ss}$/$(Ti,Mo,Si)_{ss}$ were determined for all alloys under AC and DS condition and are listed in Table 1. As expected, λ increases for DS compared to AC due to the slower cooling rate in DS.

Besides the $(Ti,Mo,Si)_{ss}$ and $(Ti,Mo)_5Si_3$ phase, a third phase was observed in the OEu manufactured by DS. SEM-EDX indicates that this additional phase is a Ti-rich carbide, see Table 2. The C uptake is correlated to the use of a graphite crucible during DS. Ti possesses a much larger solubitiy limit for C than Mo [28,29]. That is also the reason that no carbides were found in the Eu alloy [20]. However, V_f of carbide phase is neglibile (< 1 %) compared to the $V_f(Ti,Mo,Si)_{ss}$ and $V_f(Ti,Mo)_5Si_3$ phases and was found widely scattered within the investigated specimens. Nevertheless, nano-scaled precipitates with plate-like morphology were observed in the $(Ti,Mo,Si)_{ss}$, as shown in the inset of Fig. 2**f**. These precipitates are anticipated to be Ti-rich carbides, but were not further investigated yet. The Si content determined by SEM-EDX of the $(Ti,Mo,Si)_{ss}$ phase of the OEu-bcc in AC condition (see Table 2) is higher than calculated by Pandat (4 at.% vs. 2.5 at.% respectively and difference is beyond the error caused by the measurement). This indicates, that the OEu-bcc in AC condition experienced Si supersaturation indicating DS is closer to thermodynamic equilibrium. Furthermore, a higher Ti content was found in the $(Ti,Mo,Si)_{ss}$ phase of AC compared to DS (see Table 2) and is again, indicating the implication of faster cooling rates in AC. The solidification in the present case is determined by a two-phase, three-component eutectic reaction thus, the liquid continuously changes its composition during the eutectic reaction. The orientation of the eutectic trough, see Fig. 1, leads to a significant enrichment of the liquid in Ti during solidification. By increasing cooling rates, the retardation of solidification towards Ti-rich compositions is fostered.

In Fig. 3a, the compression response for AC specimens depicts that Eu has the highest strength but fails in a brittle manner, whereas the OEu show a significant amount of plastic deformability before final failure. However, both OEu show a substantial decrease in maximum strength compared to Eu (Fig. 3a). Three reasons for these observations can be identified: (i) the lower T_s, (ii) the higher $V_f(Ti,Mo,Si)_{ss}$ (see Table 1) and (iii) a reduced solid solution strengthening caused by the lower Mo content in $(Ti,Mo,Si)_{ss}$ phase compared to Eu. The lower T_s directly
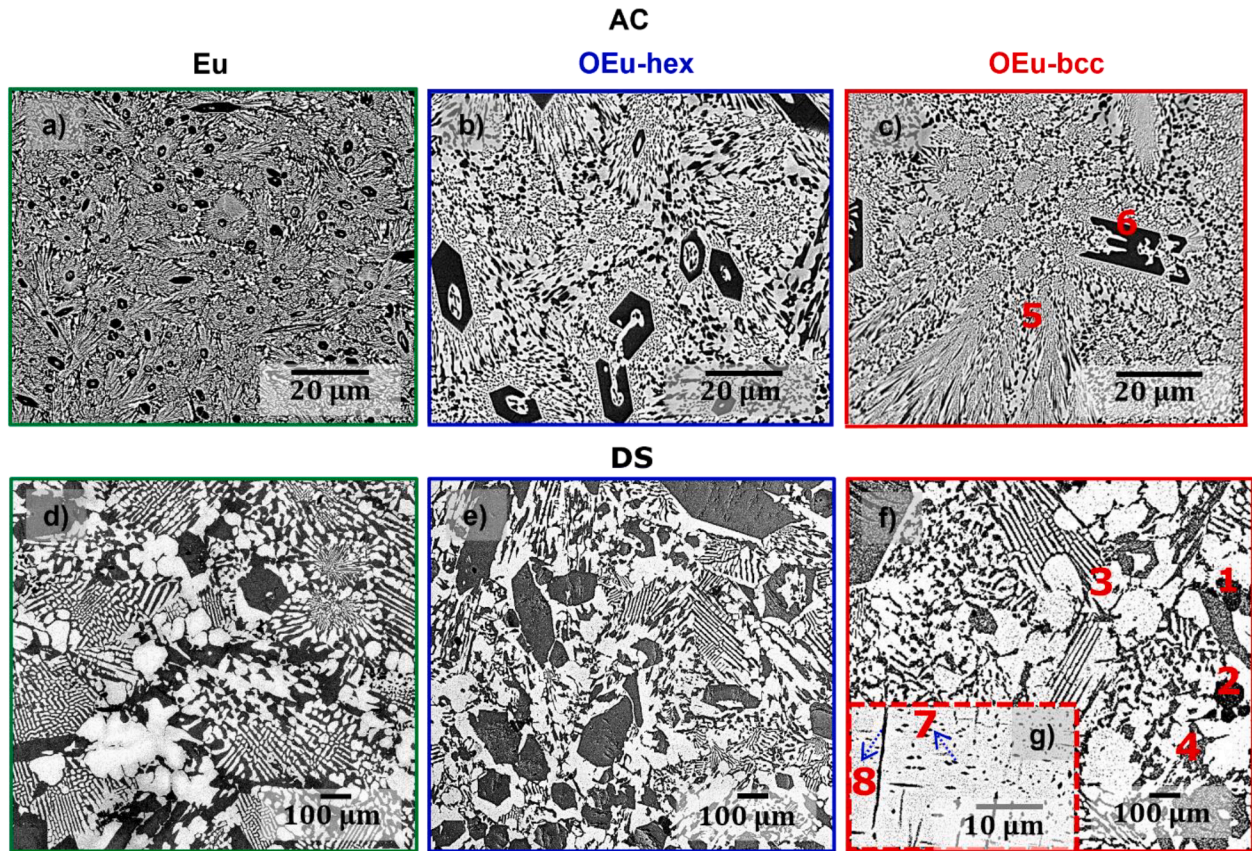
Fig. 2. SEM-BSE micrographs (transverse sections) of the Mo-Si-Ti alloys in (a-c) AC and (d-f) DS conditions. f) Presence of blocky globular dark phase revealing Ti-rich carbide phase validated by EDX (**point 1,2**) (see Table 2), the bright phase is the BCC_{ss} composed of either Mo or Ti-rich solid solution and the dark phase is the silicide phase (**point 3,4 in DS and point 5,6 in AC**), g) Inset showing the SEM-BSE micrograph of $(Ti,Mo,Si)_{ss}$ revealing silicide phase (**marked 7**) and Ti-rich carbide phase (**marked 8**).

Table 1
Strength and microstructural parameters of different alloys in AC and DS.

Parameters	Phase	Eu		OEu-hex		OEu-bcc	
		AC	DS	AC	DS	AC	DS
	Experimental: $V_f(Ti,Mo)_5Si_3$	0.45	0.43	0.42	0.42	0.39	0.39
	Pandat: $V_f(Ti,Mo)_5Si_3$	0.49	–	0.45	–	0.41	–
L / μm		0.19	2.2	0.376	1.95	0.41	2.1
λ /μm		0.34	4.3	0.75	3.9	0.82	4.2

Table 2
SEM-EDX spot analysis of the phase indicated for OEu-bcc.

Condition	Point Scan	Phase	Mo (at. %)	Ti (at. %)	Si (at. %)	C (at. %)
DS	1	**Blocky carbide**	0.1	54.5	0	45.5
	2	**Blocky carbide**	0.1	54.5	0	45.5
	3	$(Ti,Mo,Si)_{ss}$	27.1	71.2	1.7	0
	4	$(Ti,Mo)_5Si_3$	3.9	54.2	33.9	0
AC	5	$(Ti,Mo,Si)_{ss}$	15.7	80.2	4.0	0
	6	$(Ti,Mo)_5Si_3$	2.9	60.8	36.3	0

correlates to a change in homologous temperature $T_h = \frac{T}{T_s}$ for the testing conditions at 800 °C from $T_h^{Eu} = 0.48$ to $T_h^{OEu} = 0.53$. However, the change in T_h is small compared to the difference in strength from roughly 1500 MPa in Eu to 530 MPa in OEu. The lower strength of OEu in AC conditions is due to the higher Ti content in the solid solution in contrary to the Eu. A larger contribution can be attributed to the decrease of $V_f(Ti,Mo)_5Si_3$ in the OEu. As recently reported in [30], the

phases in the eutectic Mo-Si-Ti alloy form two interconnected networks. This leads to a high brittle to ductile transition temperature (BDTT) of around 1100 °C. The higher $V_f(Ti,Mo,Si)_{ss}$ would lead to a disconnected $(Ti,Mo)_5Si_3$ phase and, therefore, increases plasticity even at lower temperatures. Recently, Winkens et al. [31] reported on the solid solution strengthening in Mo-Ti alloys and found a maximum 0.2 % off set yield strength ($\sigma_{0.2}$) for (Mo,Ti) with 40 at.% Ti. This correlates directly to the composition of the $(Mo,Ti,Si)_{ss}$ phase, where the Ti content is roughly 40 at.%. However, the $(Ti,Mo,Si)_{ss}$ phase contains up to 80 at.% Ti, as confirmed by SEM-EDX (as shown in Table 2). $\sigma_{0.2}$ of $(Ti,Mo)_{ss}$ with 80 at.% Ti is about 320 MPa lower than that of $(Mo,Ti,Si)_{ss}$ according to Ref. [31]. Therefore, a significant decrease in strength can be expected by both, the increased $V_f(Ti,Mo,Si)_{ss}$ and higher Ti content in $(Ti,Mo,Si)_{ss}$.

Comparing Fig. 3a and b, yields that both OEu in DS have an increased strength compared to the AC condition, which is contrary to the trend observed for the Eu. Furthermore, Eu still fails in a brittle manner in the DS condition. Fig. 3c shows indicates a positive and negative slope $(\sigma_o/\lambda^{-0.5})$ for the Eu and OEu, respectively. To clarify the disparity of why OEu samples in DS condition display higher strength
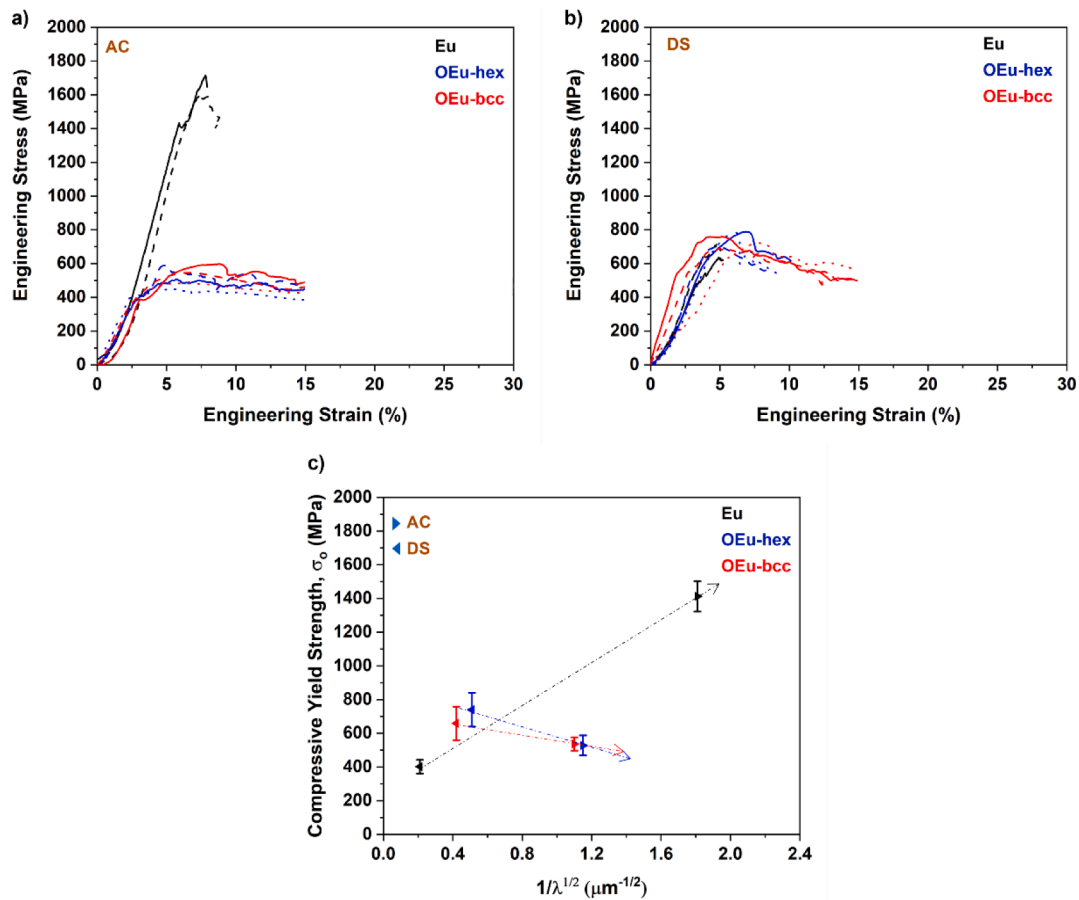
Fig. 3. a) Compression curves of Mo-Si-Ti alloys at 800 °C deliberately stopped at 15 % engineering strain for a) AC and b) DS. c) shows the trends in compressive yield strength and eutectic spacing for all three alloys in AC and DS conditions.

than their AC counterparts despite having larger microstructural length scales, it is necessary to know: (i) the amount of Ti and Si in the $(Ti,Mo,Si)_{ss}$ which leads to solid solution strengthening, the possible formation and contribution of (ii) $(Ti,Mo)_5Si_3$ precipitates in $(Ti,Mo,Si)_{ss}$ as described in Ref. [32] and iii) Ti-rich carbide phase towards strengthening.

Since the AC condition of OEu-bcc exhibits the highest amount of dissolved Si and Ti as shown in Table 2, contradicting effects can be expected by solid solution strengthening, as discussed already. Therefore, the higher Si content would result in higher strength compared to DS due to precipitation of silicide associated with intrinsic heat treatment/homogenization, while the higher Ti content will lead to lower strength contribution in AC compared to DS. However, Ref. [33] declares that Si is the most potent solid solution strengthening element in Mo. Recent investigations regarding the solid solution strengthening in bcc Ti also indicate that Si has a larger effect than Mo [34]. With this in mind, the experimental results on the strength of AC and DS condtion depends on solid solution strengthening and precipitation strengthening mechanism, which opens up avenue for broad exploration. As recently reported by Ref. [29] for the Eu, the formation of $(Ti,Mo)_5Si_3$ precipitates in $(Ti,Mo,Si)_{ss}$ was observed also in OEu, as exemplarily shown in the inset of Fig. 2f. However, the increment in strength due to precipitation strengthening might be revoked by the decrease in solid solution strengthening due to the consumption of supersaturated Si from the $(Ti,Mo,Si)_{ss}$ matrix. Recently, it was discussed in Ref. [27] that the formation and coarsening of $(Ti,Mo)_5Si_3$ precipitates in the Eu during creep at 1200 °C might contribute to the distinct creep minimum and subsequent acceleration in creep rate instead of strengthening. Therefore, we expect the major contribution for strengthening in OEu is expected by the C uptake during DS, which leads to the formation of Ti-rich

carbides within $(Ti,Mo,Si)_{ss}$. In order to asses the strengthening contribution from individual precipitate the following properties needs to be emphasized such as: 1) Hardness and Elastic Modulus, 2) Size and Distribution, 3) Coherency and Interfacial Strength and 4) Thermal Stability. Generally, Ti rich carbide typically provides higher strengthening than the Ti rich silicides [35,36]. In Ref. [37,38], it was shown that even a small fraction of carbides plays a significant role in the strength of Mo alloys. In the OEu alloy, the DS specimens undergo a strengthening balance despite increased microstructural length scale due to the formation of carbides and silicides, leading to an almost similar response to its AC counterparts. Overall, the gain in strengthening due to in-situ precipitation is greater compared to the loss of strengthening due to increased microstructural length scales due to which DS showed higher strength than the AC counterparts.

To further investigate the effect of higher strength in DS compared to AC possibly caused by the presence of nanoprecipitates, nanoindentation of the $(Ti,Mo,Si)_{ss}$ phase was performed. As seen in Fig. 4, the $(Ti,Mo,Si)_{ss}$ phase of AC experiences a larger indentation depth when compared to the $(Ti,Mo,Si)_{ss}$ phase of the DS condition. The hardness and elastic moduli for the corresponding curves are shown in Table 3, and it is higher for the $(Ti,Mo,Si)_{ss}$ of DS as compared to the AC, supporting the argument that nanoprecipitation of silicide as well as carbide particles in this phase contribute to overall strengthening. However, the order of strengthening from individual precipitate is still unclear for the present alloy system and it is our future scope to understand the mechanism, which will involve detailed nanoscopic investigation. However the most important aspect is that the combination of different nano-precipitates leads to overall strengthening.

The indentation method is used in conjunction with radial crack theory to determine and understand the fracture toughness of a phase,
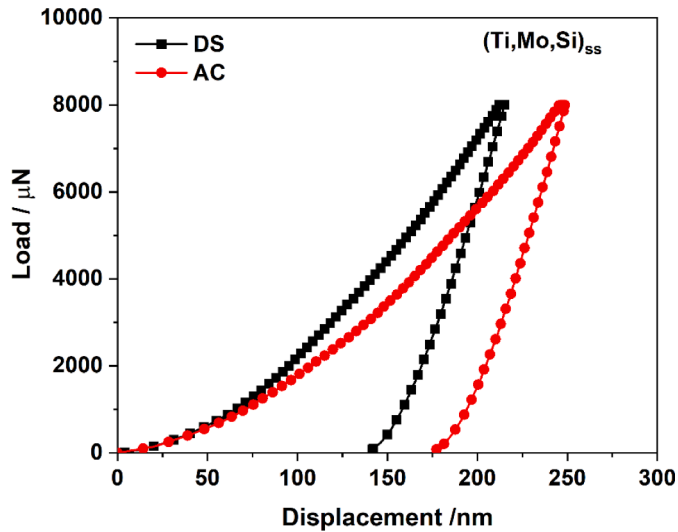
Fig. 4. The load vs. displacement curves plotted for (Ti,Mo,Si)$_{ss}$ phase in AC and DS conditions for the OEu-bcc.

Table 3
Hardness, elastic moduli trend of the (Ti,Mo,Si)$_{ss}$ phase in the OEu-bcc.

| Phase | Specimen | Mechanical Response | |
		E (GPa)	H (GPa)
(Ti,Mo,Si)$_{ss}$	**DS**	**137 ± 3**	**8.6 ± 0.3**
	AC	**127 ± 1**	**6.7 ± 0.2**

which is related to the crack size caused by a Vickers indentation as discussed by qualitatively by Hyun et al. [19] and is given by:

$$K_Q = \alpha \left(\sqrt{\frac{E}{H}} \right) \left(\frac{P_{max}}{c^{3/2}} \right) \tag{1}$$

where P$_{max}$ is the maximum indentation load, c is the radial crack length, and α is an empirical constant that depends on the geometry of the indenter tip (α = 0.016 [39])

It is well known that the presence of a ductile phase may increases the toughness of an alloy [8,9,22,40]. The overall incremental fracture toughness is strongly correlated to the product of the strength (σ_o), elastic moduli (E), volume fraction (V$_f$(Mo,Ti,Si)$_{ss}$/(Ti,Mo,Si)$_{ss}$) and the size of the ductile phase (L) (see Table 1) [27,41]. The empirical relation is given below:

$$\Delta K_Q = \sqrt{E\ C\ \sigma_o\ Vf\ (Mo, Ti, Si)ss/(Ti, Mo, Si)ss\ L} \tag{2}$$

where, ΔK$_Q$ is the incremental fracture toughness (K$_Q$ to K$_Q$ + ΔK$_Q$) due to the presence of a ductile phase. The parameter C is a constant representing the degree of constraint imposed upon a ductile phase by the brittle phase and is ~1.6 [8,24,32–35] when the ductile phase plastically deforms without interface decohesion [9,27,39,41–43].

Table 4 shows that the fracture toughness (ΔK$_Q$) enhancement is highest for DS specimens compared to AC both in Eu and OEu alloys. The

ΔK$_Q$ is lowest for AC because of its fine scale microstructure, which can lead to continuous crack propagation due to lower length scale which absorb and transmit sufficient plastic energy. The OEu alloys in DS conditions shows highest incremental fracture toughness compared to Eu and its AC counterparts. Thus directional solidification inherited with intrinsic nano-precipitation can lead a strengthend and toughneded material. According to the foregoing studies, the V$_f$(Ti,Mo)$_5$Si$_3$ is nearly 50 % and is highest in Eu and lowest in OEu, as shown in Table 1. clearly indicating DS outperforms AC microstructures.

To estimate the overall fracture toughness of the two phase microstrucure, a very large load of 10 kgf is used to generate a crack in the (Ti, Mo,Si)$_{ss}$ and the (Ti,Mo)$_5$Si$_3$ phase simultaneously and crack length was calculated radially from the indenter tip corner. The average elastic modulus and hardness are lower for OEu as compared to the Eu primarily to due to higher Ti content. From Eq. (1), the indentation fracture toughness was measured and found to be high for both OEu (around 60 MPa$\sqrt{m}$) and decreases substantially down to 18 MPa$\sqrt{m}$ for the Eu as detailed in Table 5. As observed the crack length is inversely proportional to toughness values, as shown in Fig. 5. The higher fracture toughness in OEu is presumably due to three effects: (i) the higher Ti content in the (Ti,Mo,Si)$_{ss}$ phase, (ii) the higher fraction of the (Ti,Mo, Si)$_{ss}$ phase and (iii) increased length scale of the ductile phase due to DS. As discussed before, the higher Ti content reduces the solid solution strengthening in (Ti,Mo,Si)$_{ss}$ and possibly reduce the stress for plastic deformation below the fracture stress of this phase. Previously, Ref. [30] has reported that (Mo,Ti,Si)$_{ss}$ and (Ti,Mo)$_5$Si$_3$, form 3D interconnected networks and, therefore, the brittle nature of the (Ti,Mo)$_5$Si$_3$ phase becomes dominant and comprehensible. With reducing Si in the OEu, the V$_f$ ((Mo,Ti,Si)$_{ss}$/(Ti,Mo,Si)$_{ss}$) increases and therefore the possibility that the ductile (Ti,Mo,Si)$_{ss}$ phase becomes the matrix in these alloys increases. This was not investigated in detail here. However, literature on Mo-Si-B alloys reports a change in matrix character from intermetallic to solid solution with decreasing Si content and therefore, increasing V$_f$ ((Mo,Ti,Si)$_{ss}$/(Ti,Mo,Si)$_{ss}$) [44]. The increased length scale of (Ti,Mo, Si)$_{ss}$ will contribute to increased fracture thoughtness due to the larger availability of (Mo,Ti,Si)$_{ss}$/(Ti,Mo,Si)$_{ss}$ phase, for the absorption of plastic energy as reported vikram et.al. [20].

In summary, this article presents a comprehensive exploration of novel off-eutectic Mo-Si-Ti alloys, specifically Mo-18Si-72Ti and Mo-16.5Si-72Ti, in comparison to the established eutectic Mo-20Si-52.8Ti alloy. All microstructures comprise a body-centered cubic solid solution ((Mo,Ti,Si)$_{ss}$/(Ti,Mo,Si)$_{ss}$) and silicide phase ((Ti, Mo)$_5$Si$_3$). Notably, the OEu demonstrates exceptional plastic deformability at 800 °C, distinguishing them from their Eu counterparts. Directionally solidified (DS) specimens of the OEu exhibit higher strength compared to the AC. This improved strength is attributed to the in-situ precipitation of silicide and Ti-rich carbide phase within the primary (Ti,Mo,Si)$_{ss}$ phase, despite the increase in individual phase length scales, the latter of which prove beneficial for fracture toughness via directional solidification. Thus, implementing strategic design and processing techniques leads to enhanced mechanical response with titanium playing a significant role in augmenting material properties.

Table 4
Incremental fracture toughness in three alloys in different processing conditions. σ_o is defined as the yield strength estimation of ductile phase obtained from the hardness conversion typically 2.4 HV obtained from 500 gf.

| Parameters | Eu | | OEu-hex | | OEu-bcc | |
	AC	DS	AC	DS	AC	DS
σ_o (MPa)	**1358**	**580**	**528**	**660**	**538**	**740**
ΔK$_Q$ (MPa$\sqrt{m}$)	**6.3**	**12.3**	**5.4**	**14.6**	**5.7**	**15.3**

Table 5
Indentation fracture toughness obtained for different Si-containing alloys.

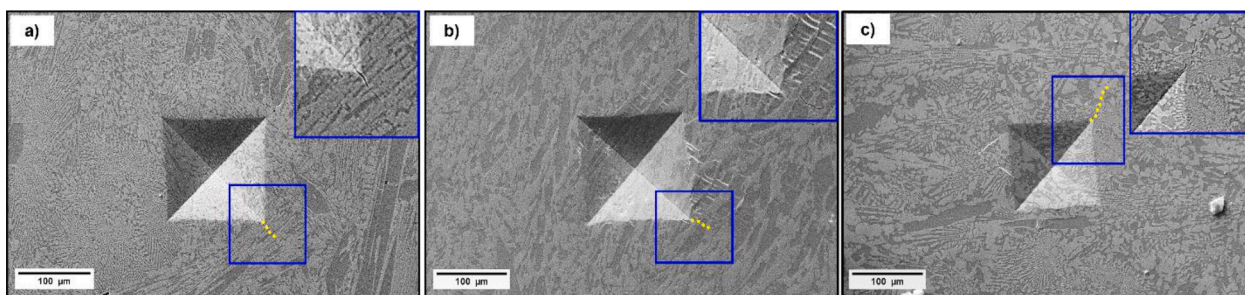| Alloy	E (GPa)	H (GPa)	E/H	P$_{max}$ (N)	c (μm)	α	K$_Q$ (MPa$\sqrt{m}$)
Eu	**180**	**6.60**	**27.27**	**98**	**58**	**0.016**	**18**
OEu-hex	**133**	**4.38**	**30.36**	**98**	**28**	**0.016**	**58**
OEu-bcc	**132**	**4.64**	**28.44**	**98**	**26**	**0.016**	**62**

Fig. 5. SEM-SE micrograph of the Vickers indentation and cracks at test loads of 10 kgf for a) OEu-bcc, b) OEu-hex, and c) Eu.

CRediT authorship contribution statement

R.J. Vikram: Writing – review & editing, Writing – original draft, Investigation, Formal analysis, Data curation, Conceptualization. **Daniel Schliephake:** Writing – review & editing, Writing – original draft, Investigation, Formal analysis. **Manoja Namadi:** Methodology, Investigation. **Abhik Choudhury:** Writing – review & editing, Supervision, Funding acquisition. **Alexander Kauffmann:** Writing – review & editing, Writing – original draft, Supervision, Formal analysis. **Satyam Suwas:** Writing – review & editing, Supervision, Funding acquisition. **Martin Heilmaier:** Writing – review & editing, Supervision, Funding acquisition.

Declaration of competing interest

The authors declare that they have no known competing financial interests or personal relationships that could have appeared to influence the work reported in this paper.

Acknowledgment

Supplementary materials

Supplementary material associated with this article can be found, in the online version, at doi:10.1016/j.scriptamat.2024.116341.

References

[1] N.L.S. Carnot, S.W. Thomson, Reflections on the Motive Power of Heat. Accompanied by an Account of Carnot's Theory, Chapman & Hall, Limited, 1897.

[2] M.J. Donachie, S.J. Donachie, Superalloys: a Technical Guide, ASM International, 2008, p. 2002.

[3] A. Bauer, S. Neumeier, F. Pyczak, M. Göken, Microstructure and creep strength of different γ/γ'- strengthened Co-base superalloy variants, Scr. Mater. 63 (2010) 1197–1200, https://doi.org/10.1016/j.scriptamat.2010.08.036.

[4] S. Praveen, H.S. Kim, High-entropy alloys: potential candidates for high-temperature applications – an overview, Adv. Eng. Mater. 20 (2018) 1–22, https://doi.org/10.1002/adem.201700645.

[5] A. Saini, T. Pollock, High-temperature materials increase efficiency of gas power plants, MRS Bull. 37 (2012) 550–551, https://doi.org/10.1557/mrs.2012.124.

[6] H. Bei, G.M. Pharr, E.P. George, A review of directionally solidified intermetaliic composites for high-temperature structural applications, J. Mater. Sci. 39 (2004) 3975–3984, https://doi.org/10.1023/B:JMSC.0000031479.32138.84.

[7] K.S. Chan, Relationships of fracture toughness and dislocation mobility in intermetallics, Metall. Mater. Trans. A Phys. Metall. Mater. Sci. 34A (2003) 2315–2328, https://doi.org/10.1007/s11661-003-0295-6.

[8] R.O. Ritchie, Mechanism of fatigue-crack propagation in ductile and brittle materials, Int. J. Fract. 100 (1998) 55–83.

[9] M.E. Launey, R.O. Ritchie, On the fracture toughness of advanced materials, Adv. Mater. 21 (2009) 2103–2110, https://doi.org/10.1002/adma.200803322.

[10] Z. Li, L.M. Peng, Microstructural and mechanical characterization of Nb-based in situ composites from Nb-Si-Ti ternary system, Acta Mater. 55 (2007) 6573–6585, https://doi.org/10.1016/j.actamat.2007.08.012.

[11] N. Sekido, Y. Kimura, S. Miura, F.G. Wei, Y. Mishima, Fracture toughness and high temperature strength of unidirectionally solidified Nb-Si binary and Nb-Ti-Si

[12] J.J. Kruzic, J.H. Schneibel, R.O. Ritchie, Fracture and fatigue resistance of Mo-Si-B alloys for ultrahigh-temperature structural applications, Scr. Mater. 50 (2004) 459–464, https://doi.org/10.1016/j.scriptamat.2003.11.002.

[13] G.A. Chadwick, Eutectic alloy solidification, Prog. Mater. Sci. 12 (1963) 99–182, https://doi.org/10.1016/0079-6425(63)90037-9.

[14] K.A. Jackson, J.D. Hunt, Lamellar and rod eutectic growth, in: P. Pelcé (Ed.), Dynamics of Curved Fronts, Academic Press, San Diego, 1988, pp. 363–376, https://doi.org/10.1016/B978-0-08-092523-3.50040-X.

[15] B. Chanda, G. Potnis, P.P. Jana, J. Das, A review on nano-/ultrafine advanced eutectic alloys, J. Alloys Compd. 827 (2020) 154226, https://doi.org/10.1016/J.JALLCOM.2020.154226.

[16] Y. Yang, Y.A. Chang, L. Tan, Y. Du, Experimental investigation and thermodynamic descriptions of the Mo-Si-Ti system, Mater. Sci. Eng. A 361 (2003) 281–293, https://doi.org/10.1016/S0921-5093(03)00560-4.

[17] D. Schliephake, A. Kauffmann, X. Cong, C. Gombola, M. Azim, B. Gorr, H.J. Christ, M. Heilmaier, Constitution, oxidation and creep of eutectic and eutectoid Mo-Si-Ti alloys, Intermetallics 104 (2019) 133–142, https://doi.org/10.1016/j.intermet.2018.10.028.

[18] Q. Lu, Y. Hao, Y. Wang, P. Feng, J. Fan, Microstructural evolution and high-temperature oxidation mechanisms of a Ti-Mo-Si composite, Corros. Sci. 161 (2019) 108180, https://doi.org/10.1016/j.corsci.2019.108180.

[19] S. Obert, A. Kauffmann, R. Pretzler, D. Schliephake, F. Hinrichs, M. Heilmaier, The creep and oxidation behaviour of pesting-resistant (Mo,ti)5si3-containing eutectic-eutectoid mo-si-ti alloys, Metals 11 (2021) 1–19, https://doi.org/10.3390/met11010169.

[20] R.J. Vikram, S.K. Aramanda, D. Schliephake, A. Kauffmann, A. Choudhury, M. Heilmaier, S. Suwas, Unveiling the intricacies of a ductile-phase toughened intermetallic: an in-depth exploration of a eutectic Mo-Si-Ti alloy and its mechanical behavior, Adv. Eng. Mater. (2024), https://doi.org/10.1002/adem.202301843.

[21] J.H. Schneibel, Mo-Si-B alloy development, in: Proceedings Og the 17th Annual Conference on Fossile Energy Materials 2003 [Baltimore, Maryland], 2003, pp. 3–9.

[22] J.A. Lemberg, R.O. Ritchie, Mo-Si-B alloys for ultrahigh-temperature structural applications, Adv. Mater. 24 (2012) 3445–3480, https://doi.org/10.1002/adma.201200764.

[23] I.J. Beyerlein, S. Xu, J. Llorca, J.A. El-Awady, J.R. Mianroodi, B. Svendsen, Alloy design for mechanical properties: conquering the length scales, MRS Bull. 44 (2019) 257–265, https://doi.org/10.1557/mrs.2019.67.

[24] C.S. Tiwary, D.R. Mahapatra, K. Chattopadhyay, Effect of length scale on mechanical properties of Al-Cu eutectic alloy, Appl. Phys. Lett. 101 (2012), https://doi.org/10.1063/1.4761944.

[25] H. Jia, X. Feng, Y. Yang, The mechanical anisotropy of directionally solidified Mg-4 wt.% Zn alloy under compression test, Mater. Sci. Eng. 762 (2019), https://doi.org/10.1016/j.msea.2019.138104.

[26] H. Bei, E.P. George, A Microstructures and mechanical properties of a directionally solidified NiAl-Mo eutectic alloy, Acta Mater. 53 (2005) 69–77, https://doi.org/10.1016/j.actamat.2004.09.003.

[27] K. Kishida, T. Maruyama, T. Fukuyama, H. Inui, Micropillar compression deformation of single crystals of α-Nb5Si3 with the tetragonal D8 l structure, Sci. Technol. Adv. Mater. 21 (2020) 805–816, https://doi.org/10.1080/14686996.2020.1855065.

[28] D. Bandyopadhyay, B. Haldar, R.C. Sharma, N. Chakraborti, The Ti-Mo-C (titanium-molybdenum-carbon) system, 2800.

[29] V.N. Eremenko, T. Va Velikanova, S.V. Shabanova, The phase diagram of the system titanium-molybdenum-carbon, n.d.

[30] A.S. Tirunilai, F. Hinrichs, D. Schliephake, M. Engstler, F. Mücklich, S. Obert, G. Winkens, A. Kauffmann, M. Heilmaier, Phase continuity, brittle to ductile transition temperature, and creep behavior of a eutectic Mo–20Si–52.8Ti alloy, Adv. Eng. Mater. 24 (2022), https://doi.org/10.1002/adem.202200918.

[31] G. Winkens, A. Kauffmann, J. Herrmann, A.K. Czerny, S. Obert, S. Seils, T. Boll, C. Baruffi, Y. Rao, W.A. Curtin, R. Schwaiger, M. Heilmaier, The influence of lattice misfit on screw and edge dislocation-controlled solid solution strengthening in Mo-Ti alloys, Commun. Mater. 4 (2023), https://doi.org/10.1038/s43246-023-00353-8.

[32] H. Thota, D. Schliephake, A. Kauffmann, H. Wu, A. Pundt, M. Heilmaier, Y. M. Eggeler, The creep-induced micro- and nanostructural evolution of a eutectic Mo-Si-Ti alloy at 1200 °C, Adv. Eng. Mater. (2024), https://doi.org/10.1002/adem.202301909.

[33] L. Northcott, Metallurgy of the Rarer Metals -5: Molybdenum, Academic Press Incorporation, New York, 1956.

[34] K. Shitara, K. Yokota, M. Yoshiya, J. Umeda, K. Kondoh, First-principles design and experimental validation of β-Ti alloys with high solid-solution strengthening and low elasticities, Mater. Sci. Eng. 843 (2022), https://doi.org/10.1016/j.msea.2022.143053.

[35] Y.I. Ryabkov, N.V. Chezhina, Y. Ryabkov, P. Istomin, N. Chezhina, Structural design and properties of layered nanocomposite titanium carbide-silicide material structural design and properties of layered nanocomposite titanium carbide-silicide materials, 2001. https://www.researchgate.net/publication/237338162.

[36] D.Y. Dang, J.L. Fan, H.R. Gong, Thermodynamic and mechanical properties of TiC from ab initio calculation, J. Appl. Phys. 116 (2014), https://doi.org/10.1063/1.4890307.

[37] H. Kwon, G.H. Gu, E.S. Kim, J. Wang, S. Son, A. Kim, J. Choi, J.H. Jeong, S. Cho, B. J. Lee, Y.U. Heo, H.S. Kim, Effect of Mo addition on the microstructure and high-specific tensile strength of Fe–Mn–Al–Ni–C ferrous medium-entropy alloy, Mater. Sci. Eng. 889 (2024), https://doi.org/10.1016/j.msea.2023.145870.

[38] T. Takahashi, T. Okazaki, Y. Furuya, Improvement in the mechanical strength of magnetostrictive (Fe-Ga-Al)-X-C (X = Zr, Nb and Mo) alloys by carbide

precipitation, Scr. Mater. 61 (2009) 5–7, https://doi.org/10.1016/j.scriptamat.2008.12.032.

[39] D. Ćorić, L. Ćurković, M.M. Renjo, Statistical analysis of vickers indentation fracture toughness of Y-TZP ceramics, Trans. Famena 41 (2017) 1–16, https://doi.org/10.21278/TOF.41201.

[40] S. Suresh, R.O. Ritchie, Propagation of short fatigue cracks, Int. Metals Rev. 29 (1984) 445–473, https://doi.org/10.1179/imtr.1984.29.1.445.

[41] M.F. Ashby, F.J. Blunt, M. Bannister, Flow characteristics of highly constrained metal wires, Acta Metall. 37 (1989) 1847–1857, https://doi.org/10.1016/0001-6160(89)90069-2.

[42] D.R. Bloyer, K.T. Venkateswara Rao, R.O. Ritchie, Fracture toughness and R-curve behavior of laminated brittle-matrix composites, Metall. Mater. Trans. A Phys. Metall. Mater. Sci. 29 (1998) 2483–2496, https://doi.org/10.1007/s11661-998-0220-0.

[43] H.C. Hyun, F. Rickhey, J.H. Lee, M. Kim, H. Lee, Evaluation of indentation fracture toughness for brittle materials based on the cohesive zone finite element method, Eng. Fract. Mech. 134 (2015) 304–316, https://doi.org/10.1016/j.engfracmech.2014.11.013.

[44] M. Krüger, S. Franz, H. Saage, M. Heilmaier, J.H. Schneibel, P. Jéhanno, M. Böning, H. Kestler, Mechanically alloyed Mo-Si-B alloys with a continuous α-Mo matrix and improved mechanical properties, Intermetallics 16 (2008) 933–941, https://doi.org/10.1016/j.intermet.2008.04.015.